Photophysics of Hybrid and Inorganic Lead Halide Perovskites

Masaru Kuno and Irina Gushchina

1 Introduction

This chapter focuses on the optoelectronic properties of hybrid and all-inorganic lead halide perovskites. Such materials adopt the chemical stoichiometry ABX_3 and are strong contenders for applications in solar photovoltaics. Among leading candidates are systems where the A cation is organic (e.g., methylammonium, $CH_3NH_3^+$, MA; formamidinium, $CH(NH_2)_2^+$, FA) or inorganic (e.g., Cs+), the B cation is Pb^{2+}, and the X anion is I^-, Br^-, or Cl^-. Important systems come from the methylammonium lead halide ($CH_3NH_3PbX_3$, or $MAPbX_3$), formamidinium lead halide [$CH(NH_2)_2PbX_3$, or $FAPbX_3$], and cesium lead halide ($CsPbX_3$) families. Alloys are also possible and $APbX_3$ materials can be produced as mixed cation, mixed anion, or even mixed cation/mixed anion alloys. Common mixed cation systems include A = FA/Cs or A = FA/MA alloys, e.g., $FA_{1-y}Cs_yPbI_3$ or $FA_{1-y}MA_yPbI_3$. Mixed anion materials are often mixtures of iodine and bromine such as $MAPb(I_{1-x}Br_x)_3$ and $FAPb(I_{1-x}Br_x)_3$ while mixed cation/anion systems include $FA_xMA_yCs_{1-x-y}Pb(I_{1-z}Br_z)_3$ (FAMACs).

Given prior discussion about the unique structural properties of ABX_3 materials, we simply recall here that $APbX_3$ perovskites adopt cubic/quasi-cubic structures at room temperature with corner sharing $[PbI_6]^{4-}$ octahedra and with A^+ cations (MA, FA, Cs) filling octahedral voids. Such structures satisfy the Goldschmidt tolerance factors required of ideal cubic structures ($0.9 \leq t \leq 1.0$) and for structures having tilted octahedra ($0.7 < t < 0.9$) [1]. The compositional diversity of mixed cation and mixed anion systems is limited by the existence of non-perovskite (δ_{ortho}- and δ_{hex}-phases) phases that appear when A^+ ionic radii are insufficient to stabilize interstitial voids in the structure [2, 3]. Although $APbX_3$ perovskites can adopt other (e.g.,

M. Kuno (✉) · I. Gushchina
University of Notre Dame, Notre Dame, IN, USA
e-mail: mkuno@nd.edu

orthorhombic) crystal structures at different temperatures [4], we focus on the photophysical properties of photovoltaically relevant cubic/pseudo-cubic structures in what follows.

The primary motivation for investigating and ultimately understanding the optical response of $APbX_3$ perovskites stems from their successful implementation in high-efficiency photovoltaics. Today, perovskite solar cell power conversion efficiencies (PCEs) routinely exceed 20%. A maximum PCE of 25.7% has been reported in NREL's benchmark efficiency chart [5] and will undoubtedly be supplanted shortly. These values collectively represent a remarkable rise of perovskite solar cell efficiencies given their modest starting value of 3.8% in 2009. In short, $APbX_3$ perovskite solar cells are, from a PCE perspective, on par with crystalline silicon.

Responsible for this success are extraordinary and fortuitous perovskite properties. This entails facile solution processability, crystallinity despite low temperature processing, chemical and stoichiometric diversity, and large absorption efficiencies, all simultaneously coupled to low exciton binding energies, large carrier mobilities, and favorable energetics to engender defect tolerance. However, despite extensive research into improving perovskite solar cell PCEs, performance bottlenecks still remain. This prevents them from reaching their full Shockley-Queisser efficiency of ~31% for single-junction devices. A need therefore exists to fully understand the fundamental optical and electrical properties of $APbX_3$ systems to realize their ultimate performance potentials.

2   Absorption

A key feature of lead halide perovskites is their favorable absorption properties. This includes sizable absorption coefficients (α), band edges close to the desired Shockley-Queisser value of 1.55 eV, and tunable absorption edges in mixed halide alloys. Figure 1a highlights these features by showing reported absorption spectra for common $APbX_3$ systems.

In the red, at approximately 1.6 eV lie $MAPbI_3$, $FAPbI_3$, and $CsPbI_3$. Near 2.2 eV are $MAPbBr_3$, $FAPbBr_3$, and $CsPbBr_3$. Further to the blue at ~3.1 eV is $MAPbCl_3$. The figure makes apparent that perovskite band gaps are sensitive to the choice of halide anion, whether I^-, Br^-, or Cl^-. This has previously suggested that the A-site cation plays a lesser role in determining the optical response of these materials. Instead, optical transitions are thought to be primarily established by perovskite's inorganic $[PbI_6]^{4-}$ framework [10]. This is supported by electronic structure calculations, which suggest A-site cation-related states being energetically removed from corresponding band edges. Cation-influenced octahedral tilting and lattice contraction [11] do, however, influence band edge energies, as evidenced by measurements on mixed cation perovskites such as $MA_{1-x}FA_xPbI_3$ or $FA_{1-x}Cs_xPbI_3$ where band gaps can be altered using cation stoichiometry [12–15].

Figure 1b further illustrates the sensitivity of perovskite band gaps to halide stoichiometry by showing how increasing the Br fraction (x) in a $MAPb(I_{1-x}Br_x)_3$ alloy

Fig. 1 Summary of the absorption spectra of various APbX$_3$ perovskites. Data extracted from References [6–9]. Spectral band edges highlighted using colored regions
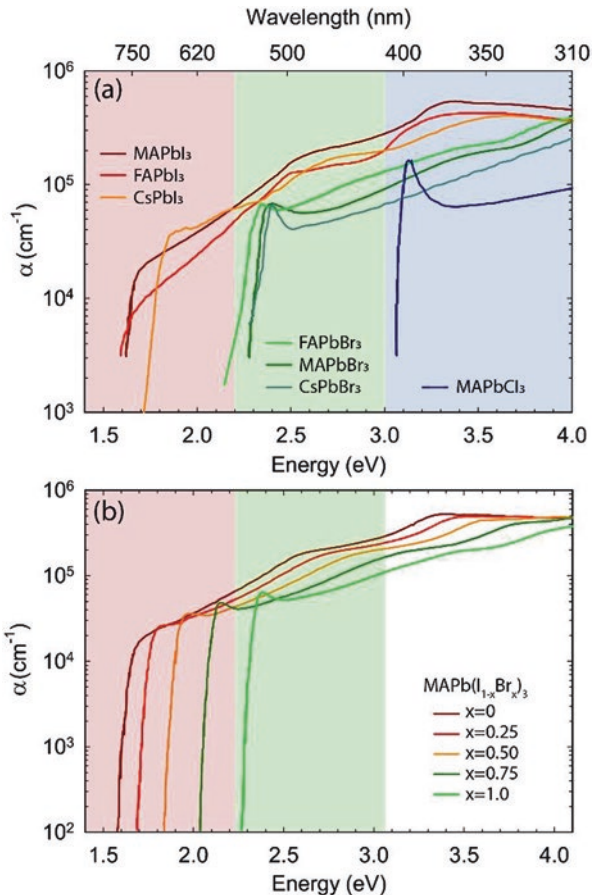
causes its E_g to progressively shift towards the MAPbBr$_3$ limit. Analogous trends are observed with MAPb(Cl$_{1-x}$Br$_x$)$_3$ [16, 17] as well as with FAPb(I$_{1-x}$Br$_x$)$_3$ [18]. The formation of continuous MAPb(I$_{1-x}$Cl$_x$)$_3$ alloys is prevented by large differences in I$^-$ and Cl$^-$ ionic radii such that little if any Cl incorporation is achieved. Consequently, such systems are denoted MAPbI$_3$(Cl) in what follows [19]. This ability to compositionally tune band gaps makes mixed halide alloys of potential use in tandem (perovskite/silicon) solar cells.

Figure 1 summarizes the absorption coefficients of these materials. Evident are sizable band edge values, which lie between 10^4 and 10^5 cm^{-1}. These α-values correspond favorably to those of other photovoltaically relevant semiconductors. To illustrate, GaAs has an absorption coefficient of $\alpha \sim 10^4$ cm^{-1} at its absorption edge. References [6, 20–22] highlight this favorable comparison by visually illustrating perovskite α-values relative to those of other semiconductors across a range of energies.

Table 1 summarizes compiled E_g and α-values for the various APbX$_3$ perovskites being discussed. Apart from the general trends noted above, there is a sizable variability in reported values. MAPbI$_3$ band gaps, for instance, range from 1.5 to

Table 1 Absorption parameters of various lead halide perovskites

System	E_g (eV)	E_b (meV)	$\alpha_{2.0\,eV}$ ($\times 10^5$ cm^{-1})	$\alpha_{2.3\,eV}$ ($\times 10^5$ cm^{-1})	$\alpha_{3.1\,eV}$ ($\times 10^5$ cm^{-1})
MAPbI$_3$	~1.5 [23]	1.7–2.1 [31]	0.23 [24, 32]	0.47 [32]	1.09 [29]
	1.55 [24, 25]	6 [41]	0.24 [21]	0.51 [29]	2.04 [25]
	1.553 [26]	7.4 [42]	0.26 [29]	0.53 [24]	2.34 [21]
	1.557 [27]	9 [43]	0.38 [31, 55]	0.59 [21]	2.43 [58]
	1.56 [28, 29]	12.3 [40]	0.39 [36]	0.64 [31, 33]	2.56 [24, 35]
	1.574 [30]	13.1 [44]	0.44 [56]	0.86 [36]	2.76 [31]
	1.59 [21, 31]	14–18 [45]	0.45 [26]	0.91 [58]	2.80 [32]
	1.6 [32–35]	16–22 [46]	0.46 [23]	0.93 [25]	2.86 [26]
	1.61 [36–38]	25 [47]	0.47 [33, 35]	0.94 [55]	2.89 [23]
	1.63 [39]	29 [48]	0.50 [57]	0.95 [35]	2.94 [33]
	1.646 [40]	32 [49]	0.58 [58]	1.01 [23]	2.99 [28]
		37 [50]	0.60 [20]	1.04 [20, 26]	3.02 [59]
		40 [51]	0.66 [30, 38]	1.19 [56]	3.15 [36]
		45 [52]	0.67 [20]	1.22 [38]	3.24 [37]
		50 [53]	0.68 [25]	1.34 [59]	3.31 [38]
		55 [54]	0.73 [39]	1.39 [46]	3.33 [56]
			0.75 [59]	1.44 [39]	3.38 [55]
			0.78 [46]	1.47 [30]	3.51 [46]
			0.79 [37]	1.50 [37]	3.68 [39]
			0.92 [28]	1.55 [28]	4.19 [34]
			1.70 [34]	2.88 [34]	4.51 [30]
FAPbI$_3$	1.45 [22]	8.4 [40]	0.25 [55]	0.71 [55]	3.59 [55]
	1.55 [55]	10 [60]	0.43 [22]	1.62 [22]	4.52 [22]
	1.566 [40]	31.6 [61]			
CsPbI$_3$	1.738 [8]	20 [62]	–	0.71 [8]	2.34 [8]
FAPbBr$_3$	2.351 [40]	24 [60]	–	0.74 [63]	1.86 [63]
		31.8 [40]			
MAPbBr$_3$	2.24 [24]	14 [65]	–	0.08 [55]	0.73 [64]
	~2.3 [56]	30.9–36.3 [40]		0.12 [24]	1.04 [24]
	2.309 [64]	40.3 [44]		0.13 [56]	1.11 [55]
	2.384–2.392 [40]	41 [66]		0.43 [64]	1.24 [56]
		76 [53]		0.91 [63]	1.77 [63]
		150 [67]			
CsPbBr$_3$	2.3 [9]	40 [62]	–	0.02 [68]	0.78 [9]
	2.37 [68]			0.13 [9]	0.89 [69]
	2.39 [69]			0.23 [63]	1.02 [68]
	2.4 [70]			0.31 [69]	1.36 [63]
				0.57 [70]	1.45 [70]
MAPbCl$_3$	2.97 [24]	41 [71]	–	–	0.35 [24]
		50 [72]			1.0 [55]

1.646 eV. This is also true of MAPbBr$_3$ where E_g-values range from 2.24 to 2.392 eV. In either case, E_g spreads are of order 150 meV.

Associated absorption coefficients are also highly variable, as evident from tabulated α-values compiled at three different energies (2.0 eV, 2.3 eV, and 3.1 eV). In particular, Table 1 shows that MAPbI$_3$ α-values at 2.0 eV range from 0.23 to

1.70×10^5 cm^{-1}. At 2.3 eV, α-values range from 0.47 to 2.88×10^5 cm^{-1}. Analogous variations exist with other perovskites. This variability and lack of accord are summarized visually in References [6, 36, 40, and 58].

Many reasons exist for apparent differences in reported optical parameters. Much has to do with variations in sample quality that stem from the numerous approaches used to prepare perovskite thin films. They include solution deposition (doctor blading, spray coating, slot-die coating, inkjet printing, etc.), solution deposition with solvent recrystallization (two-step spin-coating or antisolvent treatment), hot casting, chemical vapor deposition, and low-pressure vapor-assisted solution processing [73, 74]. Sample quality variability is especially highlighted when thin films are compared to APbX$_3$ single crystals, which possess larger grains, reduced morphological disorder, and correspondingly reduced surface roughness [75].

Consequently, what results are thin film/single crystal specimens that possess varying degrees of crystallinity, thicknesses, apparent grain sizes, surface roughness, etc. All lead to measurement variations. Fujiwara [6], for example, attributes reported E_g and α-value variations to surface roughness that introduces significant light scattering to spectroscopic ellipsometry measurements. This degrades subsequent model extraction of perovskite optical constants (i.e., frequency-dependent refractive indices and permittivities) and leads to an underestimation of perovskite band gaps. When such surface roughness variations are explicitly accounted for, a closer agreement between researcher-reported α and E_g values is realized.

Beyond band gaps and absorption coefficients, Fig. 1 reveals other intriguing features of APbX$_3$ materials. For MAPbI$_3$, FAPbI$_3$ and CsPbI$_3$, band edges resemble those of bulk, direct gap semiconductors. No apparent excitonic features are seen. The absence of an excitonic response is corroborated by numerous estimates of their exciton binding energies (E_b), as summarized in Table 1. These estimates arise from magnetoabsorption and temperature-dependent emission and absorption measurements as well as from modeling experimental APbX$_3$ band edge absorption spectra with Elliott's model [76].

Table 1 shows a spread of reported E_b values. As with E_g and α, large variations can be seen where for MAPbI$_3$ E_b ranges from 1.7 to 55 meV. Despite this, reported binding energies are of order kT and suggest that the optical response of MAPbI$_3$ and FAPbI$_3$ can be described in terms of free carriers. This conclusion is corroborated by time-resolved emission, transient differential absorption, and THz conductivity studies [76]. Note that this is not necessarily true of Br- and Cl-based APbX$_3$ materials such as CsPbBr$_3$ or MAPbCl$_3$ where prominent band edge excitonic features are seen in the linear absorption. The suggestion is supported by their generally larger E_b-values in Table 1.

The specific origin of the optical transitions in lead halide perovskites has been the subject of numerous studies. Most entail density functional theory calculations to varying degrees of approximation [24, 36, 77]. Without delving into specifics, consensus exists that valence to conduction band transitions occurs at the R symmetry point and involves valence bands that originate from the antibonding combination of halide p and Pb(6s) orbitals. Corresponding conduction bands largely arise from Pb(6p) orbitals [77]. These bands are also responsible for above gap

transitions and produce apparent structure at higher energies. For example, a feature in the absorption spectrum of MAPbI$_3$ close to 2.5 eV (Fig. 1) is attributed to a valence/conduction band transition at the M symmetry point [24, 76, 77]. The anti-bonding nature of the APbX$_3$ valence band is supported by apparent increases in perovskite band gap with increasing temperature. This contrasts itself to the response of traditional, tetrahedrally coordinated semiconductors where band gaps decrease (increase) with increasing (decreasing) temperature.

3   Carrier Dynamics

Having briefly summarized the general absorptive properties of APbX$_3$ perovskites, we now provide insight into their carrier recombination processes, following photo-excitation. This is important since the fate of photogenerated carriers is fundamental to device operation and ultimately to their efficiencies. A kinetic model is therefore developed that qualitatively and quantitatively rationalizes the intrinsic photophys-ics of APbX$_3$ systems [47, 78]. This includes experimental observations of photolu-minescence, time-correlated emission decays, and transient differential absorption dynamics. In addition to numerical simulations, analytical approximations are pro-vided to better visualize qualitative trends in both emission intensities and time-correlated decays. Although the model does not explicitly consider device operation, interested readers may refer to Reference [79] for an extension that includes charge extracting interfaces. Such a model has been used to establish the performance bottleneck(s) of a high-efficiency FAMACs solar cell.

In general, the primary recombination processes considered are (a) bimolecular (radiative) electron-hole recombination, (b) carrier trapping, and (c) nonradiative Auger recombination. The latter is nominally only important at high carrier densi-ties, far beyond 1 sun conditions. These processes are summarized in Fig. 2 with the
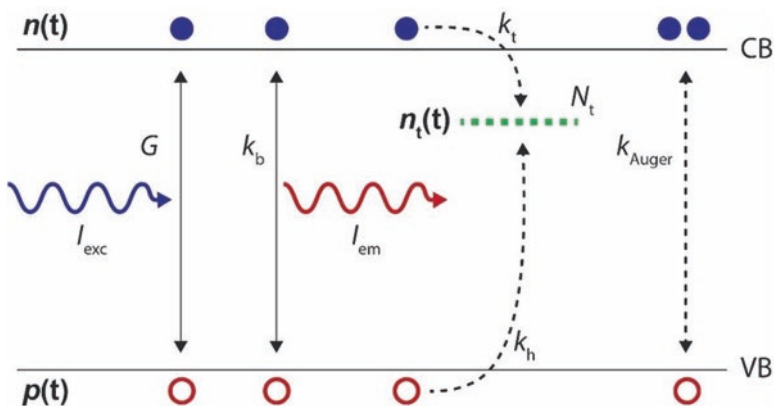

Fig. 2 Schematic illustration of photophysical processes occurring in lead halide perovskites, fol-lowing photoexcitation

illustration showing photoexcitation creating transient electron and hole populations [$n(t)$ and $p(t)$] in the perovskite conduction and valence bands. Carriers subsequently recombine via the three processes outlined above. Although the identity of $APbX_3$ trap states remains debated, there appears to be some agreement that such states are electron traps. This is assumed in what follows. Note that other versions of this model exist, which account for exciton dissociation, unintentional doping, and carrier diffusion. The interested reader is therefore referred to References [80], [81], and [49] for details.

Kinetic expressions that summarize the model are

$$\frac{dn}{dt} = G - k_t \left(N_t - n_t \right) n - k_b np - \frac{1}{2} k_{\text{Auger}} \left[n^2 p + np^2 \right]$$

$$\frac{dp}{dt} = G - k_h n_t p - k_b np - \frac{1}{2} k_{\text{Auger}} \left[n^2 p + np^2 \right]$$

$$\frac{dn_t}{dt} = k_t \left(N_t - n_t \right) n - k_h n_t p$$

$$(1)$$

where G is the initial charge generation rate (cm^{-3} s^{-1}), linked to the excitation intensity (I_{exc}, W cm^{-2}), i.e., $G = \frac{I_{\text{exc}} \alpha}{h\nu}$ with α the absorption coefficient (cm^{-1}) and $h\nu$ the photon energy (J), n (p) is the electron (hole) concentration (cm^{-3}) in the perovskite conduction (valence) band, k_t is an electron trapping rate constant (cm^3 s^{-1}), N_t is a corresponding trap density (cm^{-3}), n_t is the trap population (cm^{-3}), k_b is a bimolecular radiative recombination rate constant (cm^3 s^{-1}, referred to as k_2 in the literature), and k_{Auger} is the Auger, three-carrier rate constant (cm^6 s^{-1}, referred to as k_3 in the literature).

Numerous studies now provided estimates for the various rate constants in Eq. (1) and Fig. 2. These literature estimates are summarized in Table 2 across various $APbX_3$ systems. An inspection shows that most work has focused on $MAPbI_3$ and $MAPbI_3(Cl)$ thin films with relatively less work carried out on corresponding FA-based materials.

Table 2 also makes apparent that while variations in rate constants exist across systems and even within a given material, there is general consistency in their values. Bimolecular radiative rate constants are of order 10^{-10} cm^3 s^{-1}, while Auger rate constants are of order 10^{-28} cm^6 s^{-1} [85]. Measured pseudo-first-order rate constants for electron trapping are of order $k_1 \sim 10^7$ s^{-1} from where corresponding k_t values are of order $k_t \sim 10^{-10}$ cm^3 s^{-1}, provided estimated trap densities of order $N_t \sim 10^{-16}$ cm^{-3}.

The general photogenerated carrier dynamics, predicted by Eq. (1) at different excitation intensities, are now illustrated. Implicit to the discussion is continuous wave (CW) excitation. An identical analysis can be conducted assuming pulsed excitation. However, this is not pursued here since common applications of perovskite materials generally entail CW excitation conditions. Interested readers may refer to References [97] and [98] for details of a pulsed excitation analysis.

Table 2 Literature rate constants for various lead halide perovskites

	MAPbI$_3$	MAPbI$_3$(Cl)	MAPbBr$_3$	FAPbI$_3$	FAPb(I$_{1-x}$Br$_x$)$_3$	FAPbBr$_3$	FAMACs
$k_1 \approx k_t N_t$ ($\times 10^7$ s^{-1})	0.091 (TOPO) [82] 0.66 [82] 0.72–1.3 [83] 1.4–1.5 [84] 1.5 [85, 86] 1.8 [87]	0.49 [84] 1.2 [85] 1.2 [88]	–	0.7 [85]	–	2.1 [85]	0.4 [89]
N_t ($\times 10^{16}$ cm^{-3})	10^{-4}–10^{-3} (emissive) [90] 0.90–86 [78] 5.0–16 [59] 6.0 [80]	<0.05 [80] <0.1–4.0 [91] 1.0 [92] 2.5 [81]	–	–	–	–	0.54–60 [79]
k_b ($\times 10^{-10}$ cm^3 s^{-1})	0.1–1.0 [86] 0.35 [82] 0.4 (TOPO) [82] 0.60 [85] 1.5 [93] 1.7 [87] 3.5 [80] 6.0 [94] 6.2–37 [83] 9.2–9.4 [84] 13 [49] 23 [95]	0.23–0.78 [91] 0.87 [84] 1.1 [85, 88] 4.9 [80] 11 [96]	4.9 [93]	1.1 [85]	1.0–30 [18] ($x = 0$–1)	11 [85]	0.30 [89]
k_{Auger} ($\times 10^{-28}$ cm^6 s^{-1})	0.37–1.3 [84] ~1 [86] 1.6 [85] 3.4 [93] ~10 [94]	0.20 [85] 0.23 [88] 0.99 [84] 3.8 [96]	13.5 [93]	0.20 [85]	0.20–1.5 [18] ($x = 0$–1)	1.5 [85]	0.01 [89]

4   Low Excitation Intensities

At low excitation intensities, carrier trapping dominates radiative recombination. Low photogenerated carrier densities further mean that nonradiative Auger pathways can be ignored. Consequently, under the assumption that the material is intrinsic, Eq. (1) reduces to

$$\frac{dn}{dt} \approx G - k_t N_t n$$

$$\frac{dp}{dt} \approx G - k_h p^2$$

The equations make apparent that at steady state $n = \dfrac{G}{k_t N_t} \propto G$ and $p = \sqrt{\dfrac{G}{k_h}} \propto \sqrt{G}$.

Since the emission rate and corresponding intensity, I_{em}, are proportional to the product of n and p, I_{em} grows with increasing I_{exc} (G) in a power law fashion. Its growth exponent is ~3/2, i.e., $I_{em} \propto G^{\frac{3}{2}}$.

Figure 3a illustrates this for the case where $N_t = 10^{16}$ cm^{-3}. Employed rate constants for the numerical simulation of Eq. (1) are $k_b = 10^{-10}$ cm^3 s^{-1}, $k_t = 10^{-9}$ cm^3 s^{-1}, $k_h = 10^{-11}$ cm^3 s^{-1}, and $k_{Auger} = 10^{-28}$ cm^6 s^{-1}. The model therefore reveals that I_{em} grows as $G^{1.6}$ at low G where recombination is primarily trap-mediated (shaded red region). Figure 3b shows identical behavior for simulations where N_t has been varied between $N_t = 10^{15}$ and 10^{18} cm^{-3}. In all cases, fit-extracted growth exponents range from $m = 1.5$ to 1.6. Of note is the increasing range of G-values where $m \sim 1.5$. This is rationalized by delayed trap saturation due to larger N_t-values.

Figure 3c shows experimental data for a MAPbI$_3$ single crystal and thin film [78] that corroborate these model predictions. Acquired over ~3 orders of magnitude in G, the data reveal $m \sim 1.5$ power law growth exponents for either material, as established by fits to low G I_{em}-values (dashed lines with fit-extracted m-values shown). Differences in the range of I_{em}-values over which $m \sim 1.5$ qualitatively agree with Fig. 3b and suggest underlying N_t-value variations between MAPbI$_3$ single crystals and thin films. Other data acquired on MAPbI$_3$ and MAPbI$_3$(Cl) over 8 orders of magnitude in G reveal identical $m \sim 1.5$ power law growth exponents at low G [47]. This further corroborates the analysis and conclusions drawn here. Note that under (low irradiance) *pulsed* excitation, analogous power law growth of the integrated emission intensity is predicted with an ideal model growth exponent of $m = 2.0$ [97, 98]. Such quadratic emission growth has previously been observed for MAPbI$_3$ and MAPbI$_3$(Cl) thin films [47].

Next, by assuming above-simplified kinetic expression for n and p, corresponding (normalized) photoluminescence decays take the form

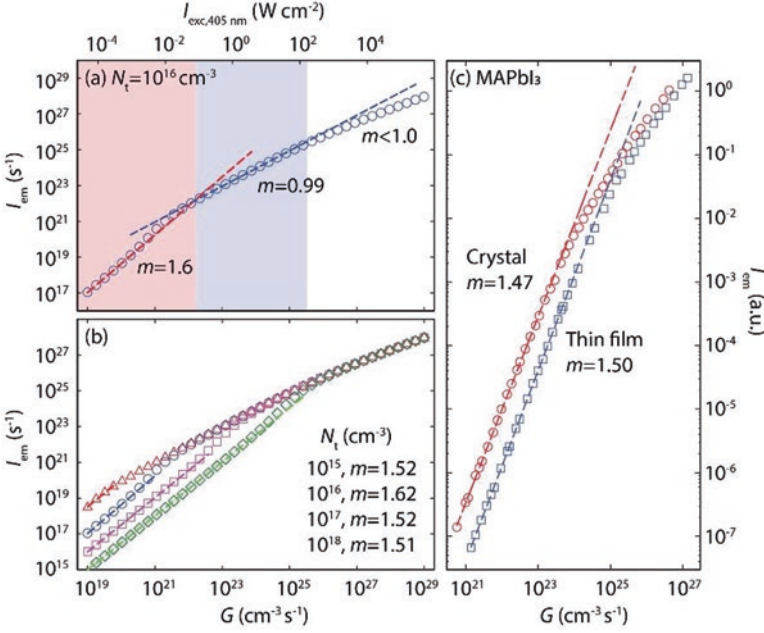$$PL(t) = \frac{I_{em}(t)}{I_{em,max}} \approx \frac{e^{-k_t N_t t}}{1 + k_h G t}. \tag{2}$$

Fig. 3 (**a**) I_{em} versus G for $N_t = 10^{16}$ cm^{-3}. Dashed lines are linear fits to the data in a given growth regime (shaded regions). Fit-extracted growth exponents shown. G-values are linked to associated I_{exc}, assuming 405 nm excitation with $\alpha = 10^5$ cm^{-1}, for reference purposes. (**b**) I_{em} versus G for N_t varying between $N_t = 10^{15}$–10^{18} cm^{-3}. Dashed lines are linear fits in the trap-mediated recombination regime. Fit-extracted growth exponents shown. (**c**) I_{em} versus G data for a MAPbI$_3$ single crystal and thin film. Data from Reference [78]. Dashed lines are fits to the data at smaller G with fit-extracted growth exponents shown

At small G or short times, the numerator in Eq. (2) dominates. Decays are therefore near exponential with an associated pseudo-first-order decay constant of $k_t N_t \sim 10^7$ s^{-1} (Table 2). Figure 4a illustrates this for the model predicted decay when $G = 10^{15}$ cm^{-3}. An accompanying (superimposed) dotted line is Eq. (2). This qualitative prediction is supported by numerous studies, which report near exponential decays at low I_{exc} for various perovskite systems [80, 81, 84, 87, 99].

5 Intermediate Excitation Intensities

As I_{exc} increases, progressive trap filling ($n_t \rightarrow N_t$) reduces the electron trapping rate such that $n \rightarrow p$. This simplifies Eq. (1) and leads to the following effective rate expressions:

$$\frac{dn}{dt} \approx G - k_b n^2$$
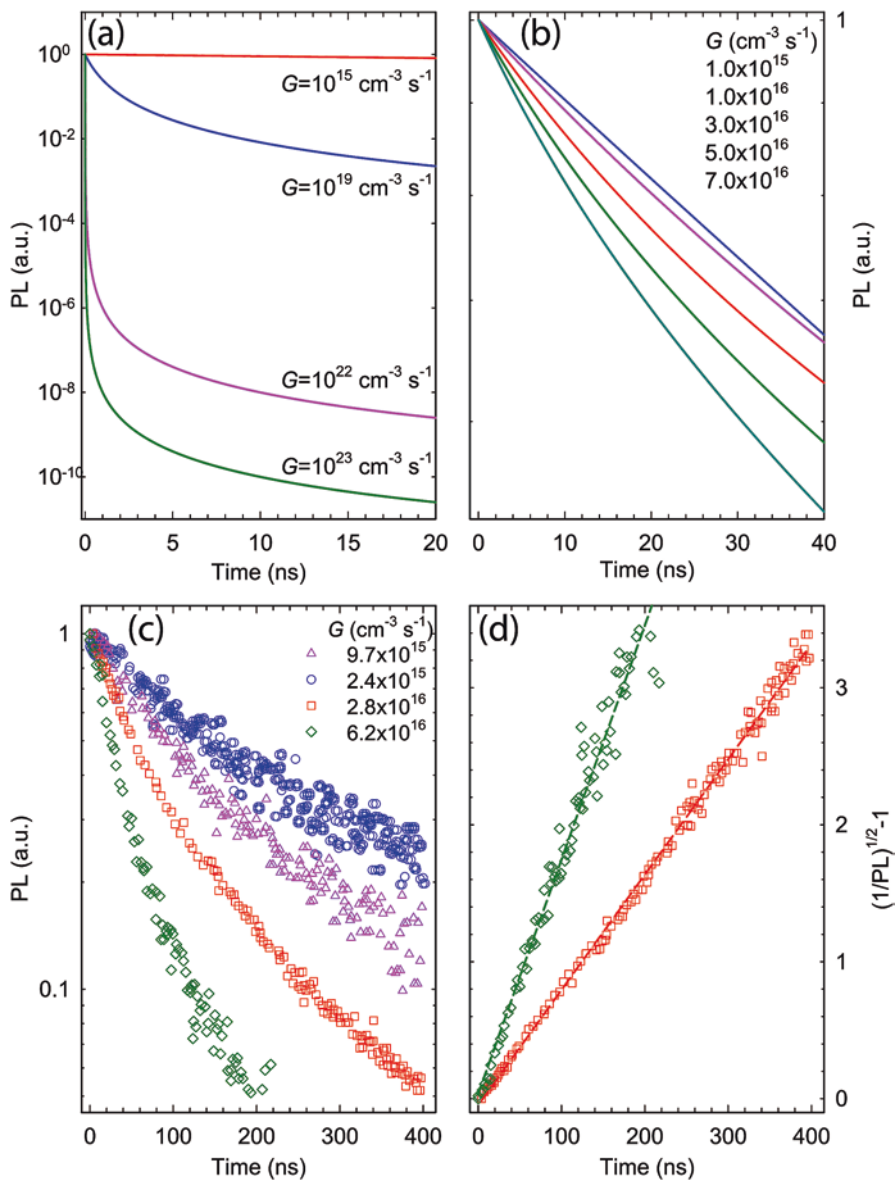
$$\frac{dp}{dt} \approx G - k_h N_t p - k_b p^2.$$

Fig. 4 (**a**) Predicted PL decays from Eq. (1) for variable G between $G = 10^{15}$ and 10^{23} cm^{-3}. Superimposed over the data are analytical predictions from Eqs. (2)–(4) (dotted lines). (**b**) Predicted decays for $G = 10^{15}$–7×10^{16} cm^{-3}. (**c**) MAPbI$_3$ PL decays from Reference [87]. (**d**) Large G MAPbI$_3$ PL decays from Reference [87] replotted. Dashed lines are linear fits to the data

Invoking steady state conditions then means that $n = \sqrt{\dfrac{G}{k_b}} \propto \sqrt{G}$ with $p = \dfrac{-k_t N_t + \sqrt{(k_t N_t)^2 + 4G}}{2} \propto \sqrt{G}$. The emission intensity therefore transitions to power law growth with a growth exponent of $m \sim 1$. Figure 3a illustrates this transition by showing a fit to the model data, highlighted in the shaded blue region. A fit-extracted power law growth exponent of $m = 0.99$ is found. Analogous behavior is observed in Fig. 3b when N_t is varied between 10^{15} and 10^{18} cm^{-3}. In whole, the model data makes evident that increasing N_t extends the region of trap-mediated recombination ($m \sim 1.5$) to larger G-values before bimolecular (radiative) recombination ($m \sim 1.0$) dominates carrier dynamics following photoexcitation.

Using the above simplified rate expressions, associated (normalized) photoluminescence decays adopt the following bimolecular form:

$$\text{PL}(t) = \frac{I_{em}(t)}{I_{em,max}} = \frac{1}{(1 + k_b G t)\left[1 + (k_t N_t + k_b G t)\right]} \tag{3}$$

where Fig. 4a shows model-predicted decays for $G = 10^{19}$ and $G = 10^{22}$ cm^{-3} using the same parameters employed earlier at low I_{exc}. Analytical results from Eq. (3) are superimposed atop the model decays and are in excellent agreement. Model decays also highlight the transition in kinetic response in this I_{exc} regime. Figure 4b illustrates this for G-values between $G = 10^{16}$ and 10^{17} cm^{-3} where for smaller G-values, near exponential behavior is seen. With increasing G, an apparent near exponential to bimolecular transition occurs. Such PL(t) transitions have previously been reported in the literature [80, 81, 87, 99] and an example from a MAPbI$_3$ thin film is shown in Fig. 4c.

6   High Excitation Intensities

At sufficiently high excitation intensities, trap saturation causes bimolecular (radiative) recombination to dominate. In this limit, Eq. (1) effectively becomes

$$\frac{dn}{dt} \approx G - k_b n^2$$

$$\frac{dp}{dt} \approx G - k_b p^2$$

so that $n = p = \sqrt{\dfrac{G}{k_b}} \propto \sqrt{G}$. I_{em} thus continues to grow in a power law fashion with a growth exponent of $m \sim 1$. Figure 3 illustrates this for $N_t = 10^{16}$ cm^{-3} (Fig. 3a) and across N_t-values between $N_t = 10^{15}$ and 10^{18} cm^{-3} (Fig. 3b). It should be mentioned that a growth exponent of $m \sim 1$ is common to this intensity regime under pulsed excitation [47, 97, 98].

An associated (normalized) photoluminescence decay takes the bimolecular form

$$\mathrm{PL}(t) = \frac{I_{em}(t)}{I_{em,max}} \approx \frac{1}{(1 + k_b G t)^2},$$

(4)

which is near identical to the expression derived earlier for intermediate excitation intensities (Eq. 3). Figure 4a plots a model-predicted decay for $G = 10^{23}$ cm^{-3} with Eq. (4) superimposed. Again, there is excellent agreement with the analytical approximation.

Beyond bimolecular fits, predicted bimolecular decays can be confirmed visually by plotting $\sqrt{\frac{I_{em,max}}{I_{em}(t)}} - 1$ versus time. In this case, linear behavior is expected [100]. Figure 4d illustrates this for the large G experimental data in Fig. 4c. Evident linear behavior is observed, as highlighted by dashed, linear fits.

Above this excitation regime, the onset of Auger-mediated nonradiative recombination causes emission efficiencies to decrease. This stems from competitive, nonradiative recombination of carriers. What results then is sublinear growth of I_{em} with an associated power law growth exponent $m < 1$. Figure 3a explicitly illustrates the onset of Auger recombination for $N_t = 10^{16}$ cm^{-3} at high G where the simulated data shows $m < 1$. It can also be shown that in this regime, plotting $\left[\frac{I_{em,max}}{I_{em}(t)} - 1\right]$ versus time yields linear behavior [100].

7 Emission Quantum Yields

Equation (1) simultaneously allows internal emission quantum yields (QYs) to be estimated through the ratio of the bimolecular radiative recombination rate to the initial carrier generation rate, i.e.

$$\mathrm{QY} = \frac{k_b n p}{G}.$$

(5)

The importance of this metric is that high emission efficiencies are requisite for optimizing APbX$_3$ photovoltaic performance. More specifically, it is the associated external quantum efficiency (EQE, EQE $= \eta_e$QY where η_e is a photon extraction efficiency) that is fundamentally linked to the maximum open circuit voltage (and PCE) achievable in a solar cell [101]. The seemingly contradictory conclusion that arises then is that a good solar cell must also be a good light emitter [102].

Figure 5 shows model-predicted (internal) QYs plotted as functions of N_t when N_t is varied between 10^{15} cm^{-3} and 10^{18} cm^{-3}. As with Figs. 3 and 4, employed rate constants have been kept constant at their nominal literature values of $k_b \sim 10^{-10}$ cm^3 s^{-1}, $k_t \sim 10^{-9}$ cm^3 s^{-1}, and $k_h \sim 10^{-11}$ cm^3 s^{-1}. Fig. 5 also provides model-predicted EQEs via $\mathrm{EQE} = \frac{\eta_e(k_b n p)}{G}$.
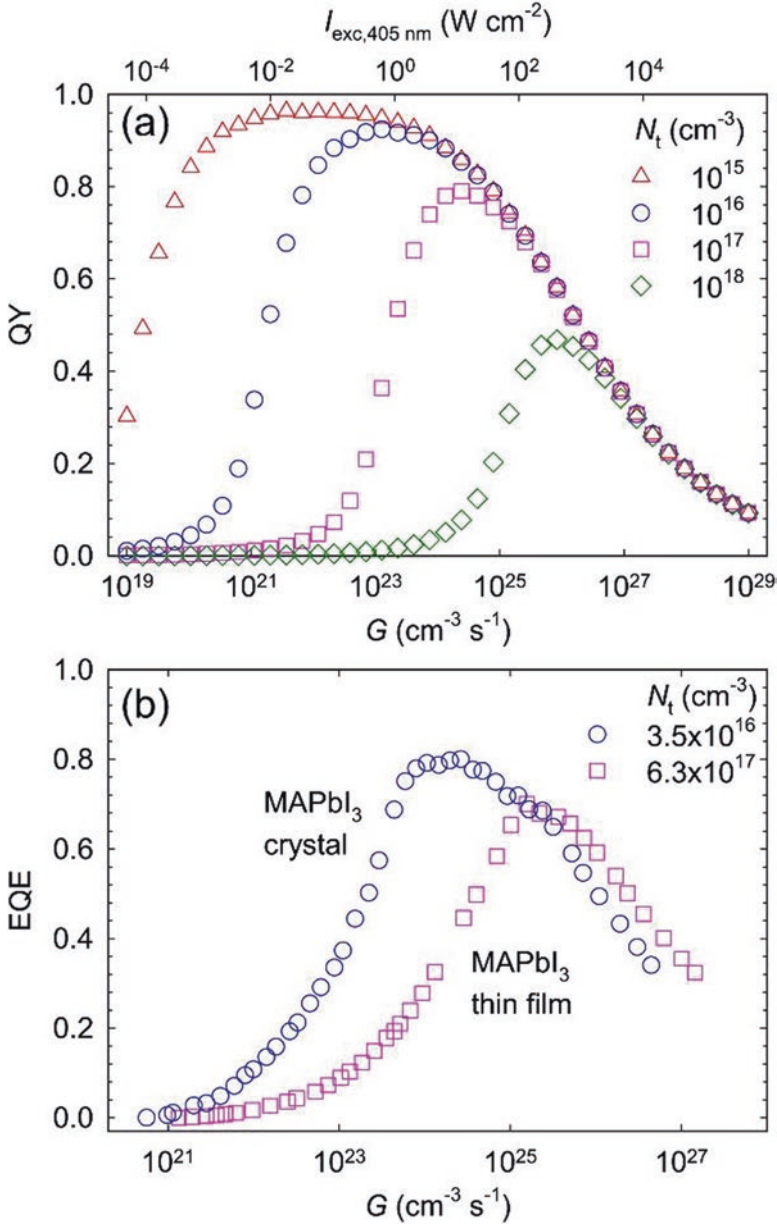
Fig. 5 (**a**) Predicted (internal) QYs for variable G between $G = 10^{19}$–10^{27} cm^{-3} and N_t between 10^{15} and 10^{18} cm^{-3}. For reference purposes, G-values are linked to associated I_{exc} assuming 405 nm excitation with $\alpha = 10^5$ cm^{-1}. (**b**) Experimental EQE estimates for a MAPbI$_3$ single crystal and thin film. Data from Reference [78]. Fit extracted N_t-values shown

Table 3 Literature APbX$_3$ emission EQEs under effective 1 sun conditions. Additives shown in parenthesis: K = potassium, Rb = rubidium, TOPO = trioctylphosphine oxide, pyr = pyridine, TPPO = triphenylphosphine oxide, SPPO = 9,9-spirobifluoren-2-yl-diphenyl-phosphine oxide)

Material	EQE film (%)	EQE film treated (%)	EQE device (%)
MAPbI$_3$	0.92 [103] 3 [82] 5 [104] 5.8 [78] 10 [105]	12–13 (TOPO) [106] 20.3 (TOPO) [103] 35 (TOPO) [82]	5 [106]
MAPbI$_3$(Cl)	20 [104] 50–60 [107]	24–25 (pyr) [108]	–
MAPbBr$_3$	2–3 [109] 15 [104]	1.2 [110] 32 (TPPO) [111] 85 (SPPO) [111]	–
FAMACs	2.4 [112] 66 (K) [113]	3.6 (Rb) [112]	0.43–2.83 [79] 14.5 (K) [113]
FAMAPb(I$_{1-x}$Br$_x$)$_3$	-	-	0.1–3.0 [114]

The resulting figure illustrates several things. First, as discussed earlier, at low I_{exc}, trapping dominates carrier recombination. This leads to low QYs. Attesting to this are experimental perovskite, 1 sun EQEs in Table 3. Values for thin films, (surface) treated thin films, and devices are shown. Inspection of the data reveals that reported 1 sun EQEs are generally on the order of several percent with some notable exceptions. This is consistent with the lower QYs seen at low G in Fig. 5. Of note is that this bulk perovskite data contrasts itself to analogous results, summarized in Reference [115] for perovskite nanocrystals (NCs). In these materials, EQEs regularly approach or attain unity values.

Next, Table 3 shows that treating lead halide perovskite thin films with Lewis bases such as trioctylphosphine oxide (TOPO) or pyridine improves their EQEs. However, they only increase values to numbers of order 10%. This indicates that while defect passivation is possible, significant trap densities still remain. This is again unlike the case of perovskite NCs where effective surface passivation does appear possible and which leads to unity EQEs [116]. Finally, Table 3 shows that device EQEs are all suppressed from corresponding thin film or treated thin film values due to the inevitable competition for carriers by electron and hole extraction interfaces present in working devices.

Figure 5 shows that maximal QYs are achieved upon trap saturation at high excitation intensities. In the case where $N_t = 10^{16}$ cm^{-3}, near unity internal QYs are realized close to 1 sun conditions. The figure further shows that increasing N_t simply leads to progressively larger I_{exc}-values required to achieve peak QYs, which themselves become progressively smaller. In all cases, maximum QYs persist until a critical G beyond which the onset of Auger-mediated carrier recombination causes them to fall as discussed earlier.

This QY behavior has previously been modeled by reducing the kinetics in Eq. (1) to [85].

$$\frac{dN}{dt} = G - AN - BN^2 - CN^3.$$

(6)

In Eq. (6), N is an effective electron-hole density, A is a generic first-order rate constant that describes nonradiative, trap-mediated recombination of photogenerated carriers, B is a second-order (radiative) rate constant, and C is a third-order rate constant that accounts for nonradiative Auger recombination. The rate constants A, B, and C are effectively k_1, k_b, and k_{Auger} in Table 2. A corresponding internal QY is then

$$QY = \frac{BN^2}{AN + BN^2 + CN^3}.$$

(7)

Equation (7) can be recast in terms of EQE via $EQE = \frac{\eta_e BN^2}{AN + \eta_e BN^2 + CN^3}$. In either case, a peak QY can be found by taking the derivative of QY (EQE) with respect to N to find a critical point (i.e., $\frac{dQY}{dN} = \frac{dEQE}{dN} = 0$) [85]. A resulting optimal carrier density (N_{opt}) is then

$$N_{opt} = \sqrt{\frac{A}{C}} \sim \sqrt{\frac{k_1}{k_{Auger}}}$$

(8)

and is linked to a corresponding maximum internal QY of

$$QY_{max} = \frac{1}{1 + \frac{2\sqrt{AC}}{B}} \sim \frac{1}{1 + \frac{2\sqrt{k_1 k_{Auger}}}{k_2}}$$

(9)

with a corresponding maximum EQE of $EQE_{max} = \frac{1}{1 + \frac{2\sqrt{AC}}{\eta_e B}} \sim \frac{1}{1 + \frac{2\sqrt{k_1 k_{Aug}}}{\eta_e k_2}}$.

Equations (6) and (7) can be used to model experimental EQEs to extract relevant rate constants. They are, however, not predictive in that tabulated rate constants from Table 2 cannot be used to estimate QYs and EQE a priori. This is because Figs. 3–5 show that trap saturation occurs due to $n_t \rightarrow N_t$. Consequently, the pseudo-first-order trapping rate constant (here A) is I_{exc}-dependent. Immediate application of Eqs. (8) and (9) therefore leads to predicted N_{opt} and QY_{max} smaller than those revealed by full numerical simulations of Eq. (1) (Fig. 5).

Finally, beyond trap-mediated recombination, an important reason for small overall EQE values and for why EQEs are smaller than internal QYs is photon trapping within the perovskite. This originates from refractive index differences with the surrounding medium and is most prominent in APbX$_3$ films and crystals where physical sizes approach the wavelength of light. This leads to estimated photon extraction efficiencies of $\eta_e \sim 10\%$ [104, 105]. Note that such trapping is not significant for NCs as they effectively behave as dipole emitters. This rationalizes why unity/near unity EQEs are readily seen with these materials [115].

8   Ion Migration

Finally, despite all of the notable properties of APbX$_3$ materials, preventing their widespread commercialization is their well-known environmental sensitivities. Addressing this have been a number of studies [117, 118]. Less recognized but equally important are intrinsic instabilities linked to ion migration. Namely, both cations and anions in APbX$_3$ materials are mobile with ion mobilities stemming from vacancy-mediated ion migration under bias or under illumination.

For cations, evidence for bias-induced A$^+$ migration comes from observed device hysteresis thought to stem from cation accumulation at electrodes [119–121]. The phenomenon is better illustrated using more direct measurements such as time-of-flight secondary ion mass spectrometry and super-resolution infrared absorption measurements [122, 123], which explicitly reveal cation migration and accumulation near electrodes.

For anions, a well-known phenomenon is light-induced photosegregation whereby shining light on mixed I$^-$/Br$^-$ systems [e.g., MAPb(I$_{1-x}$Br$_x$)$_3$] induces halide segregation. This results in the formation of I-rich inclusions within parent, mixed halide perovskites. Such photoinduced halide segregation is experimentally observed as progressive photoluminescence redshifts due to photogenerated carriers being funneled to I-rich domains. Such domains act as emissive recombination centers because of favorable (valence) band offsets relative to those of parent mixed halide materials. Observed redshifts/photosegregation are reversible when specimens are no longer illuminated with remixing being entropically driven. References [4, 124, and 125] provide more details on the phenomenon.

At this point, an inevitable question that arises is the connection between the earlier photocarrier dynamics and the bias−/light-induced ion migration described here. Since ion migration, whether cation or anion, is thought to be vacancy-mediated and since point defects are likely responsible for carrier trapping, a connection between the two is suggested. Evidence for this can already be found in the literature where References [126, 127, and 128] already suggest that decreasing defect densities mitigates ion migration. Studies linking the two topics, however, are limited. Consequently, more work is required to establish a comprehensive picture of ion-inclusive carrier dynamics that follow photoexcitation of APbX$_3$ systems. As such, linking the two sets the direction for future investigations of these unique materials.

References

1. Goldschmidt, V. (1926). Die Gesetze der Krystallochemie. *Die Naturwissenschaften, 14*, 477–485.
2. Manser, J., Christians, J., & Kamat, P. (2016). Intriguing optoelectronic properties of metal halide perovskites. *Chemical Reviews, 116*, 12956–13008.
3. Stoumpos, C., & Kanatzidis, M. (2015). The renaissance of halide perovskites and their evolution as emerging semiconductors. *Accounts of Chemical Research, 48*, 2791–2802.
4. Brennan, M., Ruth, A., Kamat, P., & Kuno, M. (2020). Photoinduced anion segregation in mixed halide perovskites. *Trends in Chemistry, 2*, 282–301.
5. Best research-cell efficiency chart [Internet]. Nrel.gov. 2022 [cited 26 January 2022]. Available from https://www.nrel.gov/pv/cell-efficiency.html.
6. Fujiwara, H., Kato, M., Tamakoshi, M., Miyadera, T., & Chikamatsu, M. (2018). Optical characteristics and operational principles of hybrid perovskite solar cells. *Physica Status Solidi (a), 215*, 1700730.
7. Fujiwara, H., & Collins, R. W. (2018). Organic-inorganic hybrid perovskites. *Spectroscopic Ellipsometry for Photovoltaics, 2*, 471–493.
8. Yan, W., Guo, Y., Beri, D., Dottermusch, S., Chen, H., & Richards, B. S. (2020). Experimental determination of complex optical constants of air-stable inorganic $CsPbI_3$ perovskite thin films. *Physica Status Solidi (RRL)–Rapid Research Letters, 14*, 2000070.
9. Yan, W., Mao, L., Zhao, P., Mertens, A., Dottermusch, S., Hu, H., Jin, Z., & Richards, B. S. (2020). Determination of complex optical constants and photovoltaic device design of all-inorganic $CsPbBr_3$ perovskite thin films. *Optics Express, 28*, 15706–15717.
10. Chen, H., Lee, M., & Chen, C. (2016). Wavelength-dependent optical transition mechanisms for light-harvesting of perovskite $MAPbI_3$ solar cells using first-principles calculations. *Journal of Materials Chemistry C, 4*, 5248–5254.
11. Prasanna, R., Gold-Parker, A., Leijtens, T., Conings, B., Babayigit, A., Boyen, H. G., Toney, M. F., & McGehee, M. D. (2017). Band gap tuning via lattice contraction and octahedral tilting in perovskite materials for photovoltaics. *Journal of the American Chemical Society, 139*, 11117–11124.
12. Pellet, N., Gao, P., Gregori, G., Yang, T., Nazeeruddin, M., Maier, J., & Grätzel, M. (2014). Mixed-organic-cation perovskite photovoltaics for enhanced solar-light harvesting. *Angewandte Chemie International Edition, 53*, 3151–3157.
13. Ono, L., Juarez-Perez, E., & Qi, Y. (2017). Progress on perovskite materials and solar cells with mixed cations and halide anions. *ACS Applied Materials & Interfaces, 9*, 30197–30246.
14. Li, Z., Yang, M., Park, J., Wei, S., Berry, J., & Zhu, K. (2015). Stabilizing perovskite structures by tuning tolerance factor: Formation of formamidinium and cesium lead iodide solid-state alloys. *Chemistry of Materials, 28*, 284–292.
15. Weber, O., Charles, B., & Weller, M. T. (2016). Phase behaviour and composition in the formamidinium–methylammonium hybrid lead iodide perovskite solid solution. *Journal of Materials Chemistry A, 4*, 15375–15382.
16. Sadhanala, A., Ahmad, S., Zhao, B., Giesbrecht, N., Pearce, P., Deschler, F., Hoye, R. L. Z., Gödel, K. C., Bein, T., Docampo, P., Dutton, S. E., De Volder, M. F. L., & Friend, R. H. (2015). Blue-green color tunable solution processable organolead chloride–bromide mixed halide perovskites for optoelectronic applications. *Nano Letters, 15*, 6095–6101.
17. Tang, S., Xiao, X., Hu, J., Gao, B., Chen, H., Peng, Z., Wen, J., Era, M., & Zou, D. (2020). Solvent-free mechanochemical synthesis of a systematic series of pure-phase mixed-halide perovskites $MAPb(I_xBr_{1-x})_3$ and $MAPb(Br_xCl_{1-x})_3$ for continuous composition and band-gap tuning. *ChemPlusChem, 85*, 240–246.
18. Rehman, W., Milot, R. L., Eperon, G. E., Wehrenfennig, C., Boland, J. L., Snaith, H. J., Johnston, M. B., & Herz, L. M. (2015). Charge-carrier dynamics and mobilities in formamidinium lead mixed-halide perovskites. *Advanced Materials, 27*, 7938–7944.

19. Colella, S., Mosconi, E., Fedeli, P., Listorti, A., Gazza, F., Orlandi, F., Ferro, P., Besagni, T., Rizzo, A., Calestani, G., Gigli, G., De Angelis, F., Mosca, R., & Gigli, G. (2013). MAPbI$_{3-x}$Cl$_x$ mixed halide perovskite for hybrid solar cells: The role of chloride as dopant on the transport and structural properties. *Chemistry of Materials, 25*, 4613–4618.

20. De Wolf, S., Holovsky, J., Moon, S. J., Löper, P., Niesen, B., Ledinsky, M., Haug, F. J., Yum, J. H., & Ballif, C. (2014). Organometallic halide perovskites: Sharp optical absorption edge and its relation to photovoltaic performance. *Journal of Physical Chemistry Letters, 5*, 1035–1039.

21. Ziang, X., Shifeng, L., Laixiang, Q., Shuping, P., Wei, W., Yu, Y., Li, Y., Zhijian, C., Shufeng, W., Honglin, D., Minghui, Y., & Qin, G. G. (2015). Refractive index and extinction coefficient of CH$_3$NH$_3$PbI$_3$ studied by spectroscopic ellipsometry. *Optical Materials Express, 5*, 29–43.

22. Xie, Z., Sun, S., Yan, Y., Zhang, L., Hou, R., Tian, F., & Qin, G. G. (2017). Refractive index and extinction coefficient of NH$_2$CH=NH$_2$PbI$_3$ perovskite photovoltaic material. *Journal of Physics: Condensed Matter, 29*, 245702.

23. Ghimire, K., Cimaroli, A., Hong, F., Shi, T., Podraza, N., & Yan, Y.. (2015, June 14). Spectroscopic ellipsometry studies of CH$_3$NH$_3$PbX$_3$ thin films and their growth evolution. In *2015 IEEE 42nd Photovoltaic Specialist Conference (PVSC)* (pp. 1–5). IEEE.

24. Leguy, A. M., Azarhoosh, P., Alonso, M. I., Campoy-Quiles, M., Weber, O. J., Yao, J., Bryant, D., Weller, M. T., Nelson, J., Walsh, A., Van Schilfgaarde, M., & Barnes, P. R. F. (2016). Experimental and theoretical optical properties of methylammonium lead halide perovskites. *Nanoscale, 8*, 6317–6327.

25. Phillips, L. J., Rashed, A. M., Treharne, R. E., Kay, J., Yates, P., Mitrovic, I. Z., Weerakkody, A., Hall, S., & Durose, K. (2016). Maximizing the optical performance of planar CH$_3$NH$_3$PbI$_3$ hybrid perovskite heterojunction stacks. *Solar Energy Materials and Solar Cells, 147*, 327–233.

26. Loper, P., Stuckelberger, M., Niesen, B., Werner, J., Filipic, M., Moon, S. J., Yum, J. H., Topic, M., De Wolf, S., & Ballif, C. (2015). Complex refractive index spectra of CH$_3$NH$_3$PbI$_3$ perovskite thin films determined by spectroscopic ellipsometry and spectrophotometry. *Journal Physical Chemistry Letters, 6*, 66–71.

27. Manzoorm, S., Häusele, J., Bush, K. A., Palmstrom, A. F., Carpenter, J., Zhengshan, J. Y., Bent, S. F., Mcgehee, M. D., & Holman, Z. C. (2018). Optical modeling of wide-bandgap perovskite and perovskite/silicon tandem solar cells using complex refractive indices for arbitrary-bandgap perovskite absorbers. *Optics Express, 26*, 27441–27460.

28. Ball, J. M., Stranks, S. D., Hörantner, M. T., Hüttner, S., Zhang, W., Crossland, E. J., Ramirez, I., Riede, M., Johnston, M. B., Friend, R. H., & Snaith, H. J. (2015). Optical properties and limiting photocurrent of thin-film perovskite solar cells. *Energy & Environmental Science, 8*, 602–609.

29. Marronnier, A., Lee, H., Lee, H., Kim, M., Eypert, C., Gaston, J. P., Roma, G., Tondelier, D., Geffroy, B., & Bonnassieux, Y. (2018). Electrical and optical degradation study of methylammonium-based perovskite materials under ambient conditions. *Solar Energy Materials and Solar Cells, 178*, 179–185.

30. Bailey, C. G., Piana, G. M., & Lagoudakis, P. G. (2019). High-energy optical transitions and optical constants of CH$_3$NH$_3$PbI$_3$ measured by spectroscopic ellipsometry and spectrophotometry. *Journal of Physical Chemistry C, 123*, 28795–28801.

31. Lin, Q., Armin, A., Nagiri, R. C., Burn, P. L., & Meredith, P. (2015). Electro-optics of perovskite solar cells. *Nature Photonics, 9*, 106–112.

32. Leguy, A. M., Hu, Y., Campoy-Quiles, M., Alonso, M. I., Weber, O. J., Azarhoosh, P., Van Schilfgaarde, M., Weller, M. T., Bein, T., Nelson, J., Docampo, P., & Barnes, P. R. F. (2015). Reversible hydration of CH$_3$NH$_3$PbI$_3$ in films, single crystals, and solar cells. *Chemistry of Materials, 27*, 3397–3407.

33. Wang, Z., Yuan, S., Li, D., Jin, F., Zhang, R., Zhan, Y., Lu, M., Wang, S., Zheng, Y., Guo, J., Fan, Z., & Chen, L. (2016). Influence of hydration water on CH$_3$NH$_3$PbI$_3$ perovskite films prepared through one-step procedure. *Optics Express, 24*, A1431–A1443.

34. Wang, X., Gong, J., Shan, X., Zhang, M., Xu, Z., Dai, R., Wang, Z., Wang, S., Fang, X., & Zhang, Z. (2018). In situ monitoring of thermal degradation of CH$_3$NH$_3$PbI$_3$ films by spectroscopic ellipsometry. *Journal of Physical Chemistry C, 123*, 1362–1369.

35. Demchenko, D. O., Izyumskaya, N., Feneberg, M., Avrutin, V., Özgür, Ü., Goldhahn, R., & Morkoç, H. (2016). Optical properties of the organic-inorganic hybrid perovskite CH$_3$NH$_3$PbI$_3$: Theory and experiment. *Physical Review B, 94*, 075206.

36. Shirayama, M., Kadowaki, H., Miyadera, T., Sugita, T., Tamakoshi, M., Kato, M., Fujiseki, T., Murata, D., Hara, S., Murakami, T. N., Fujimoto, S., Chikamatsu, M., & Fujiwara, H. (2016). Optical transitions in hybrid perovskite solar cells: Ellipsometry, density functional theory, and quantum efficiency analyses for CH$_3$NH$_3$PbI$_3$. *Physical Review Applied, 5*, 014012.

37. Jiang, Y., Soufiani, A. M., Gentle, A., Huang, F., Ho-Baillie, A., & Green, M. A. (2016). Temperature dependent optical properties of CH$_3$NH$_3$PbI$_3$ perovskite by spectroscopic ellipsometry. *Applied Physics Letters, 108*, 061905.

38. Guerra, J. A., Tejada, A., Korte, L., Kegelmann, L., Töfflinger, J. A., Albrecht, S., Rech, B., & Weingärtner, R. (2017). Determination of the complex refractive index and optical bandgap of CH$_3$NH$_3$PbI$_3$ thin films. *Journal of Applied Physics, 121*, 173104.

39. Ghimire, K., Zhao, D., Cimaroli, A., Ke, W., Yan, Y., & Podraza, N. J. (2016). Optical monitoring of CH$_3$NH$_3$PbI$_3$ thin films upon atmospheric exposure. *Journal of Physics D: Applied Physics, 49*, 405102.

40. Green, M. A., Jiang, Y., Soufiani, A. M., & Ho-Baillie, A. (2015). Optical properties of photovoltaic organic–inorganic lead halide perovskites. *Journal Physical Chemistry Letters, 6*, 4774–4785.

41. Yamada, Y., Nakamura, T., Endo, M., Wakamiya, A., & Kanemitsu, Y. (2015). Photoelectronic responses in solution-processed perovskite CH$_3$NH$_3$PbI$_3$ solar cells studied by photoluminescence and photoabsorption spectroscopy. *IEEE Journal of Photovoltaics, 5*, 2156–3381.

42. Ziffer, M., Mohammed, J., & Ginger, D. S. (2016). Electroabsorption spectroscopy measurements of the exciton binding energy, electron–hole reduced effective mass, and band gap in the perovskite CH$_3$NH$_3$PbI$_3$. *ACS Photonics, 3*, 1060–1068.

43. Yang, Y., Ostrowski, D., France, R., Zhu, K., van de Lagemaat, J., Luther, J., & Beard, M. C. (2015). Observation of a hot-phonon bottleneck in lead-iodide perovskites. *Nature Photonics, 10*, 53–59.

44. Yang, Y., Yang, M., Li, Z., Crisp, R., Zhu, K., & Beard, M. C. (2015). Comparison of recombination dynamics in CH$_3$NH$_3$PbBr$_3$ and CH$_3$NH$_3$PbI$_3$ perovskite films: influence of exciton binding energy. *Journal of Physical Chemistry Letters, 6*, 4688–4692.

45. Miyata, A., Mitioglu, A., Plochocka, P., Portugall, O., Wang, J., Stranks, S., Snaith, H. J., & Nicholas, R. J. (2015). Direct measurement of the exciton binding energy and effective masses for charge carriers in organic–inorganic tri-halide perovskites. *Nature Physics, 11*, 582–587.

46. Sun, S., Salim, T., Mathews, N., Duchamp, M., Boothroyd, C., Xing, G., Sum, T. S., & Lam, Y. M. (2014). The origin of high efficiency in low-temperature solution-processable bilayer organometal halide hybrid solar cells. *Energy & Environmental Science, 7*, 399–407.

47. Saba, M., Cadelano, M., Marongiu, D., Chen, F., Sarritzu, V., Sestu, N., Figus, C., Aresti, M., Piras, R., Lehmann, A. G., Cannas, C., Musinu, A., Quochi, F., Mura, A., & Bongiovanni, G. (2014). Correlated electron–hole plasma in organometal perovskites. *Nature Communications, 5*, 5049.

48. Sestu, N., Cadelano, M., Sarritzu, V., Chen, F., Marongiu, D., Piras, R., Mainas, M., Quochi, F., Saba, M., Mura, A., & Bongiovanni, G. (2015). Absorption f-sum rule for the exciton binding energy in methylammonium lead halide perovskites. *Journal of Physical Chemistry Letters, 6*, 4566–4572.

49. Savenije, T. J., Ponseca, C. S., Jr., Kunneman, L., Abdellah, M., Zheng, K., Tian, Y., Zhu, Q., Canton, S. E., Scheblykin, I. G., Pullerits, T., Yartsev, A., & Sundström, V. (2014). Thermally activated exciton dissociation and recombination control the carrier dynamics in organometal halide perovskite. *Journal of Physical Chemistry Letters, 5*, 2189–2194.

50. Hirasawa, M., Ishihara, T., & Goto, T. (1994). Exciton features in 0-, 2-, and 3-dimensional networks of $[PbI_6]^{4-}$octahedra. *Journal of the Physical Society of Japan, 63*, 3870–3879.

51. Zhu, X., Su, H., Marcus, R., & Michel-Beyerle, M. E. (2014). Computed and experimental absorption spectra of the perovskite $CH_3NH_3PbI_3$. *Journal of Physical Chemistry Letters, 5*, 3061–3065.

52. Ishihara, T. (1994). Optical properties of PbI-based perovskite structures. *Journal of Luminescence, 60-61*, 269–274.

53. Tanaka, K., Takahashi, T., Ban, T., Kondo, T., Uchida, K., & Miura, N. (2003). Comparative study on the excitons in lead-halide-based perovskite-type crystals $CH_3NH_3PbBr_3$ $CH_3NH_3PbI_3$. *Solid State Communications, 127*(9–10), 619–623.

54. D'Innocenzo, V., Grancini, G., Alcocer, M., Kandada, A., Stranks, S. D., Lee, M. M., Lanzani, G., Snaith, H. J., & Petrozza, A. (2014). Excitons versus free charges in organo-lead tri-halide perovskites. *Nature Communications, 5*, 3586.

55. Kato, M., Fujiseki, T., Miyadera, T., Sugita, T., Fujimoto, S., Tamakoshi, M., Chikamatsu, M., & Fujiwara, H. (2017). Universal rules for visible-light absorption in hybrid perovskite materials. *Journal of Applied Physics, 121*, 115501.

56. Park, J. S., Choi, S., Yan, Y., Yang, Y., Luther, J. M., Wei, S. H., Parilla, P., & Zhu, K. (2015). Electronic structure and optical properties of α-$CH_3NH_3PbBr_3$ perovskite single crystal. *Journal of Physical Chemistry Letters, 6*, 4304–4308.

57. Xing, G., Mathews, N., Sun, S., Lim, S., Lam, Y., Grätzel, M., Mhaisalkar, S., & Sum, T. C. (2013). Long-range balanced electron- and hole-transport lengths in organic-inorganic $CH_3NH_3PbI_3$. *Science, 342*, 344–347.

58. Jiang, Y., Green, M. A., Sheng, R., & Ho-Baillie, A. (2015). Room temperature optical properties of organic–inorganic lead halide perovskites. *Solar Energy Materials and Solar Cells, 137*, 253–257.

59. Xing, G., Mathews, N., Lim, S. S., Yantara, N., Liu, X., Sabba, D., Grätzel, M., Mhaisalkar, S., & Sum, T. C. (2014). Low-temperature solution-processed wavelength-tunable perovskites for lasing. *Nature Materials, 13*, 476–480.

60. Galkowski, K., Mitioglu, A., Miyata, A., Plochocka, P., Portugall, O., Eperon, G., Wang, J., Stergiopoulos, J., Stranks, S., Snaith, H. J., & Nicholas, R. J. (2016). Determination of the exciton binding energy and effective masses for methylammonium and formamidinium lead tri-halide perovskite semiconductors. *Energy & Environmental Science, 9*, 962–970.

61. Liu, Y., Wang, J., Zhu, N., Liu, W., Wu, C., Liu, C., Xiao, L., Chen, Z., & Wang, S. (2019). Investigation on binding energy and reduced effective mass of exciton in organic–inorganic hybrid lead perovskite films by a pure optical method. *Optics Letters, 44*, 3474–3477.

62. Protesescu, L., Yakunin, S., Bodnarchuk, M., Krieg, F., Caputo, R., Hendon, C., Yang, R. X., Walsh, A., & Kovalenko, M. V. (2015). Nanocrystals of cesium lead halide perovskites $(CsPbX_3$, X = Cl, Br, and I): Novel optoelectronic materials showing bright emission with wide color gamut. *Nano Letters, 15*, 3692–3696.

63. Mannino, G., Deretzis, I., Smecca, E., La Magna, A., Alberti, A., Ceratti, D., & Cahen, D. (2020). Temperature-dependent optical band gap in $CsPbBr_3$, $MAPbBr_3$, and $FAPbBr_3$ single crystals. *Journal of Physical Chemistry Letters, 11*, 2490–2496.

64. Alias, M. S., Dursun, I., Saidaminov, M. I., Diallo, E. M., Mishra, P., Ng, T. K., Bakr, O. M., & Ooi, B. S. (2016). Optical constants of $CH_3NH_3PbBr_3$ perovskite thin films measured by spectroscopic ellipsometry. *Optics Express, 24*, 16586–16594.

65. Awasthi, K., Du, K., Wang, C., Tsai, C., Hamada, M., Narra, S., Diau, E., & Ohta, N. (2018). Electroabsorption studies of multicolored lead halide perovskite nanocrystalline solid films. *ACS Photonics, 5*, 2408–2417.

66. Ruf, F., Aygüler, M., Giesbrecht, N., Rendenbach, B., Magin, A., Docampo, P., Kalt, H., & Hetterich, M. (2019). Temperature-dependent studies of exciton binding energy and phase-transition suppression in (Cs,FA,MA)Pb(I,Br)$_3$ perovskites. *APL Materials, 7*, 031113.

67. Koutselas, I., Ducasse, L., & Papavassiliou, G. C. (1996). Electronic properties of three- and low-dimensional semiconducting materials with Pb halide and Sn halide units. *Journal of Physics: Condensed Matter, 8*, 1217–1227.

68. Chen, C., Wu, D., Yuan, M., Yu, C., Zhang, J., Li, C., & Duan, Y. (2021). Spectroscopic ellipsometry study of CsPbBr$_3$ perovskite thin films prepared by vacuum evaporation. *Journal of Physics D: Applied Physics, 54*, 224002.

69. Zhao, M., Shi, Y., Dai, J., & Lian, J. (2018). Ellipsometric study of the complex optical constants of a CsPbBr$_3$ perovskite thin film. *Journal of Materials Chemistry C, 6*, 10450–10455.

70. Chen, X., Wang, Y., Song, J., Li, X., Xu, J., Zeng, H., & Sun, H. (2019). Temperature dependent reflectance and ellipsometry studies on a CsPbBr$_3$ single crystal. *Journal of Physical Chemistry C, 123*, 10564–10570.

71. Yamada, T., Aharen, T., & Kanemitsu, Y. (2018). Near-band-edge optical responses of CH$_3$NH$_3$PbCl$_3$ single crystals: Photon recycling of excitonic luminescence. *Physical Review Letters, 120*, 057404.

72. Comin, R., Walters, G., Thibau, E., Voznyy, O., Lu, Z., & Sargent, E. H. (2015). Structural, optical, and electronic studies of wide-bandgap lead halide perovskites. *Journal of Materials Chemistry C, 3*, 8839–8843.

73. Abbas, M., Zeng, L., Guo, F., Rauf, M., Yuan, X., & Cai, B. (2020). A critical review on crystal growth techniques for scalable deposition of photovoltaic perovskite thin films. *Materials, 13*, 4851.

74. Saki, Z., Byranvand, M., Taghavinia, N., Kedia, M., & Saliba, M. (2021). Solution-processed perovskite thin-films: The journey from lab- to large-scale solar cells. *Energy & Environmental Science, 14*, 5690–5722.

75. Trivedi, S., Prochowicz, D., Parikh, N., Mahapatra, A., Pandey, M., Kalam, A., Tavakoli, M. M., & Yadav, P. (2021). Recent progress in growth of single-crystal perovskites for photovoltaic applications. *ACS Omega, 6*, 1030–1042.

76. Herz, L. M. (2016). Charge-carrier dynamics in organic-inorganic metal halide perovskites. *Annual Review of Physical Chemistry, 67*, 65–89.

77. Even, J., Pedesseau, L., Katan, C., Kepenekian, M., Lauret, J. S., Sapori, D., & Deleporte, E. (2015). Solid-state physics perspective on hybrid perovskite semiconductors. *Journal of Physical Chemistry C, 119*, 10161–10177.

78. Draguta, S., Thakur, S., Morozov, Y. V., Wang, Y., Manser, J. S., Kamat, P. V., & Kuno, M. (2016). Spatially non-uniform trap state densities in solution-processed hybrid perovskite thin films. *Journal of Physical Chemistry Letters, 7*, 715–721.

79. Draguta, S., Christians, J. A., Morozov, Y. V., Mucunzi, A., Manser, J. S., Kamat, P. V., Luther, J. M., & Kuno, M. (2018). A quantitative and spatially resolved analysis of the performance-bottleneck in high efficiency, planar hybrid perovskite solar cells. *Energy & Environmental Science, 11*, 960–969.

80. Hutter, E. M., Eperon, G. E., Stranks, S. D., & Savenije, T. J. (2015). Charge carriers in planar and meso-structured organic–inorganic perovskites: Mobilities, lifetimes, and concentrations of trap states. *Journal of Physical Chemistry Letters, 6*, 3082–3090.

81. Stranks, S. D., Burlakov, V. M., Leijtens, T., Ball, J. M., Goriely, A., & Snaith, H. J. (2014). Recombination kinetics in organic-inorganic perovskites: Excitons, free charge, and subgap states. *Physical Review Applied, 2*, 034007.

82. DeQuilettes, D. W., Koch, S., Burke, S., Paranji, R. K., Shropshire, A. J., Ziffer, M. E., & Ginger, D. S. (2016). Photoluminescence lifetimes exceeding 8 μs and quantum yields exceeding 30% in hybrid perovskite thin films by ligand passivation. *ACS Energy Letters, 1*, 438–444.

83. D'Innocenzo, V., Srimath Kandada, A. R., De Bastiani, M., Gandini, M., & Petrozza, A. (2014). Tuning the light emission properties by band gap engineering in hybrid lead halide perovskite. *Journal of the American Chemical Society, 136*, 17730–17733.

84. Wehrenfennig, C., Eperon, G. E., Johnston, M. B., Snaith, H. J., & Herz, L. M. (2014). High charge carrier mobilities and lifetimes in organolead trihalide perovskites. *Advanced Materials, 26*, 1584–1589.

85. Johnston, M. B., & Herz, L. M. (2016). Hybrid perovskites for photovoltaics: Charge-carrier recombination, diffusion, and radiative efficiencies. *Accounts of Chemical Research, 49*, 146–154.

86. Milot, R. L., Eperon, G. E., Snaith, H. J., Johnston, M. B., & Herz, L. M. (2015). Temperature-dependent charge-carrier dynamics in CH$_3$NH$_3$PbI$_3$ perovskite thin films. *Advanced Functional Materials, 25*, 6218–6227.

87. Yamada, Y., Nakamura, T., Endo, M., Wakamiya, A., & Kanemitsu, Y. (2014). Photocarrier recombination dynamics in perovskite CH$_3$NH$_3$PbI$_3$ for solar cell applications. *Journal of the American Chemical Society, 136*, 11610–11613.

88. Wehrenfennig, C., Liu, M., Snaith, H. J., Johnston, M. B., & Herz, L. M. (2014). Charge-carrier dynamics in vapour-deposited films of the organolead halide perovskite CH$_3$NH$_3$PbI$_{3-x}$Cl$_x$. *Energy & Environmental Science, 7*, 2269–2275.

89. Wolff, C. M., Bourelle, S. A., Phuong, L. Q., Kurpiers, J., Feldmann, S., Caprioglio, P., Marquez, J. A., Wolansky, J., Unold, T., Stolterfoht, M., Shoaee, S., Deschler, F., & Neher, D. (2021). Orders of recombination in complete perovskite solar cells-linking time-resolved and steady-state measurements. *Advanced Energy Materials, 45*, 2101823.

90. Dobrovolsky, A., Merdasa, A., Li, J., Hirselandt, K., Unger, E. L., & Scheblykin, I. G. (2020). Relating defect luminescence and nonradiative charge recombination in MAPbI$_3$ perovskite films. *Journal of Physical Chemistry Letters, 11*, 1714–1720.

91. de Quilettes, D. W., Vorpahl, S. M., Stranks, S. D., Nagaoka, H., Eperon, G. E., Ziffer, M. E., Snaith, H. J., & Ginger, D. S. (2015). Impact of microstructure on local carrier lifetime in perovskite solar cells. *Science, 348*, 683–686.

92. Samiee, M., Konduri, S., Ganapathy, B., Kottokkaran, R., Abbas, H. A., Kitahara, A., Joshi, P., Zhang, L., Noack, M., & Dalal, V. (2014). Defect density and dielectric constant in perovskite solar cells. *Applied Physics Letters, 105*, 153502.

93. Chen, X., Lu, H., Yang, Y., & Beard, M. C. (2018). Excitonic effects in methylammonium lead halide perovskites. *Journal of Physical Chemistry Letters, 9*, 2595–2603.

94. Guo, Z., Manser, J. S., Wan, Y., Kamat, P. V., & Huang, L. (2015). Spatial and temporal imaging of long-range charge transport in perovskite thin films by ultrafast microscopy. *Nature Communications, 6*, 7471.

95. Manser, J. S., & Kamat, P. V. (2014). Band filling with free charge carriers in organometal halide perovskites. *Nature Photonics, 8*, 737–743.

96. Trinh, M. T., Wu, X., Niesner, D., & Zhu, X. Y. (2015). Many-body interactions in photo-excited lead iodide perovskite. *Journal of Materials Chemistry A, 3*, 9285–9290.

97. Vietmeyer, F., Frantsuzov, P. A., Janko, B., & Kuno, M. (2011). Carrier recombination dynamics in individual CdSe nanowires. *Physical Review B, 83*, 115319.

98. Morozov, Y. V., Draguta, S., Zhang, S., Cadranel, A., Wang, Y., Janko, B., & Kuno, M. (2017). Defect-mediated CdS nanobelt photoluminescence up-conversion. *Journal of Physical Chemistry C, 121*, 16607–16616.

99. Stranks, S. D. (2017). Nonradiative losses in metal halide perovskites. *ACS Energy Letters, 2*, 1515–1525.

100. Puthussery, J., Lan, A., Kosel, T. H., & Kuno, M. (2008). Band-filling of solution-synthesized CdS nanowires. *ACS Nano, 2*, 357–367.

101. Ross, R. T. (1967). Some thermodynamics of photochemical systems. *The Journal of Chemical Physics, 46*, 4590–4593.

102. Miller, O. D., Yablonovitch, E., & Kurtz, S. R. (2012). Strong internal and external luminescence as solar cells approach the Shockley–Queisser limit. *IEEE Journal of Photovoltaics, 2*, 303–311.

103. Braly, I. L., de Quilettes, D. W., Pazos-Outón, L. M., Burke, S., Ziffer, M. E., Ginger, D. S., & Hillhouse, H. W. (2018). Hybrid perovskite films approaching the radiative limit with over 90% photoluminescence quantum efficiency. *Nature Photonics, 12*, 355–361.

104. Richter, J. M., Abdi-Jalebi, M., Sadhanala, A., Tabachnyk, M., Rivett, J. P., Pazos-Outón, L. M., Gödel, K. C., Price, M., Deschler, F., & Friend, R. H. (2016). Enhancing photoluminescence yields in lead halide perovskites by photon recycling and light out-coupling. *Nature Communications, 7*, 13941.

105. Pazos-Outón, L. M., Szumilo, M., Lamboll, R., Richter, J. M., Crespo-Quesada, M., Abdi-Jalebi, M., Beeson, H. J., Vrućinić, M., Alsari, M., Snaith, H. J., Ehrler, B., Friend, R. H., & Deschler, F. (2016). Photon recycling in lead iodide perovskite solar cells. *Science, 351*, 1430–1433.

106. Liu, Z., Krückemeier, L., Krogmeier, B., Klingebiel, B., Márquez, J. A., Levcenko, S., Öz, S., Mathur, S., Rau, U., Unold, T., & Kirchartz, T. (2018). Open-circuit voltages exceeding 1.26 V in planar methylammonium lead iodide perovskite solar cells. *ACS Energy Letters, 4*, 110–117.

107. Deschler, F., Price, M., Pathak, S., Klintberg, L. E., Jarausch, D. D., Higler, R., Hüttner, S., Leijtens, T., Stranks, S. D., Snaith, H. J., Atatüre, M., Phillips, R. T., & Friend, R. H. (2014). High photoluminescence efficiency and optically pumped lasing in solution-processed mixed halide perovskite semiconductors. *Journal of Physical Chemistry Letters, 5*, 1421–1426.

108. Noel, N. K., Abate, A., Stranks, S. D., Parrott, E. S., Burlakov, V. M., Goriely, A., & Snaith, H. J. (2014). Enhanced photoluminescence and solar cell performance via Lewis base passivation of organic–inorganic lead halide perovskites. *ACS Nano, 8*, 9815–9821.

109. Kojima, K., Ikemura, K., Matsumori, K., Yamada, Y., Kanemitsu, Y., & Chichibu, S. F. (2019). Internal quantum efficiency of radiation in a bulk $CH_3NH_3PbBr_3$ perovskite crystal quantified by using the omnidirectional photoluminescence spectroscopy. *APL Materials, 7*, 071116.

110. Droseros, N., Longo, G., Brauer, J., Sessolo, M., Bolink, H., & Banerji, N. (2018). Origin of the enhanced photoluminescence quantum yield in $MAPbBr_3$ perovskite with reduced crystal size. *ACS Energy Letters, 3*, 1458–1466.

111. Longo, G., La-Placa, M., Sessolo, M., & Bolink, H. J. (2017). High photoluminescence quantum yields in organic semiconductor-perovskite composite thin films. *ChemSusChem, 10*, 3788–3793.

112. Saliba, M., Matsui, T., Domanski, K., Seo, J. Y., Ummadisingu, A., Zakeeruddin, S. M., Correa-Baena, J. P., Tress, W. R., Abate, A., Hagfeldt, A., & Grätzel, M. (2016). Incorporation of rubidium cations into perovskite solar cells improves photovoltaic performance. *Science, 354*, 206–209.

113. Abdi-Jalebi, M., Andaji-Garmaroudi, Z., Cacovich, S., Stavrakas, C., Philippe, B., Richter, J. M., Alsari, M., Booker, E. P., Hutter, E. M., Pearson, A. J., Lilliu, S., Savenije, T. J., Rensmo, H., Divitini, G., Ducati, C., Friend, R. H., & Stranks, S. D. (2018). Maximizing and stabilizing luminescence from halide perovskites with potassium passivation. *Nature, 555*, 497–501.

114. Kramarenko, M., Ferreira, C. G., Martínez-Denegri, G., Sansierra, C., Toudert, J., & Martorell, J. (2020). Relation between fluorescence quantum yield and open-circuit voltage in complete perovskite solar cells. *Solar RRL, 4*, 1900554.

115. Zhang, S., Zhukovskyi, M., Jankó, B., & Kuno, M. (2019). Progress in laser cooling semiconductor nanocrystals and nanostructures. *NPG Asia Materials, 11*, 1–9.

116. Koscher, B. A., Swabeck, J. K., Bronstein, N. D., & Alivisatos, A. P. (2017). Essentially trap-free $CsPbBr_3$ colloidal nanocrystals by postsynthetic thiocyanate surface treatment. *Journal of the American Chemical Society, 139*, 6566–6569.

117. Mazumdar, S., Zhao, Y., & Zhang, X. (2021). Stability of perovskite solar cells: Degradation mechanisms and remedies. *Frontiers in Electronics, 2*, 712785.

118. Wang, R., Mujahid, M., Duan, Y., Wang, Z., Xue, J., & Yang, Y. (2019). A review of perovskites solar cell stability. *Advanced Functional Materials, 29*, 1808843.

119. Futscher, M., Lee, J., McGovern, L., Muscarella, L., Wang, T., Haider, M. C., Fakharuddin, A., Schmidt-Mende, L., & Ehrler, B. (2019). Quantification of ion migration in $CH_3NH_3PbI_3$ perovskite solar cells by transient capacitance measurements. *Materials Horizons, 6*, 1497–1503.

120. Calado, P., Telford, A., Bryant, D., Li, X., Nelson, J., O'Regan, B. C., & Barnes, P. R. (2016). Evidence for ion migration in hybrid perovskite solar cells with minimal hysteresis. *Nature Communications, 7*, 13831.

121. Singh, R., & Parashar, M. (2020). Origin of hysteresis in perovskite solar cells. In J. Ren & Z. Kan (Eds.), *Soft-Matter Thin Film Solar Cells* (pp. 1–42). AIP Publishing Books.
122. Pavlovetc, I. M., Brennan, M. C., Draguta, S., Ruth, A., Moot, T., Christians, J. A., Aleshire, K., Harvey, S. P., Toso, S., Nanayakkara, S. U., Messinger, J., Luther, J. M., & Kuno, M. (2020). Suppressing cation migration in triple-cation lead halide perovskites. *ACS Energy Letters, 5*, 2802–2810.
123. Lin, Y., Chen, B., Fang, Y., Zhao, J., Bao, C., Yu, Z., Deng, Y., Rudd, P. N., Yan, Y., Yuan, Y., & Huang, J. (2018). Excess charge-carrier induced instability of hybrid perovskites. *Nature Communications, 9*, 4981.
124. Brennan, M. C., Draguta, S., Kamat, P. V., & Kuno, M. (2017). Light-induced anion phase segregation in mixed halide perovskites. *ACS Energy Letters, 3*, 204–213.
125. Wang, Y., Quintana, X., Kim, J., Guan, X., Hu, L., Lin, C. H., Jones, B. T., Chen, W., Wen, X., Gao, H., & Wu, T. (2020). Phase segregation in inorganic mixed-halide perovskites: From phenomena to mechanisms. *Photonics Research, 8*, A56–A71.
126. Zhang, G., Long, R., Lu, Y., Zhang, S., Zhao, W., Yu, Y., Mi, Q., Qin, P., & Huang, F. (2021). Calcium-assisted in situ formation of perovskite nanocrystals for luminescent green and blue emitters. *ACS Applied Nano Materials, 4*, 14303–14311.
127. Zheng, X., Yuan, S., Liu, J., Yin, J., Yuan, F., Shen, W., Yao, K., Wei, M., Zhou, C., Song, K., Zhang, B., Lin, Y., Hedhili, M. N., Wehbe, N., Han, Y., Sun, H., Lu, Z., Anthopoulos, T. D., Mohammed, O. F., Sargent, E. H., Liao, L., & Bakr, O. M. (2020). Chlorine vacancy passivation in mixed halide perovskite quantum dots by organic pseudohalides enables efficient rec. 2020 blue light-emitting diodes. *ACS Energy Letters, 5*, 793–798.
128. Wang, F., Bai, S., Tress, W., Hagfeldt, A., & Gao, F. (2018). Defects engineering for high-performance perovskite solar cells. *Npj Flexible Electronics, 2*, 22.